Article

Towards a Better Understanding of the Interaction of Fe$_{66}$Cr$_{10}$Nb$_5$B$_{19}$ Metallic Glass with Aluminum: Growth of Intermetallics and Formation of Kirkendall Porosity during Sintering

Dina V. Dudina [1,2,*] , Vyacheslav I. Kvashnin [1] , Alexander A. Matvienko [2] , Anatoly A. Sidelnikov [2] , Alexander I. Gavrilov [2], Arina V. Ukhina [2], Alberto Moreira Jorge, Jr. [3,4,5] and Konstantinos Georgarakis [6]

[1] Lavrentyev Institute of Hydrodynamics SB RAS, Lavrentyev Ave. 15, 630090 Novosibirsk, Russia
[2] Institute of Solid State Chemistry and Mechanochemistry SB RAS, Kutateladze Str. 18, 630090 Novosibirsk, Russia
[3] Department of Materials Science and Engineering, Federal University of São Carlos, ViaWashington Luiz, km 235, São Carlos 13565-905, SP, Brazil
[4] The Laboratory of Electrochemistry and Physical-Chemistry of Materials and Interfaces (LEPMI), Université Grenoble Alpes, Université Savoie Mont Blanc, CNRS, Grenoble INP, 38000 Grenoble, France
[5] Science et Ingénierie des Matériaux et Procédés (SIMaP), Université Grenoble Alpes, CNRS, Grenoble INP, 38000 Grenoble, France
[6] School of Aerospace, Transport and Manufacturing, Cranfield University, Cranfield MK43 0AL, UK
[*] Correspondence: dina1807@gmail.com

Abstract: Metallic-glass-reinforced metal matrix composites are a novel class of composite materials, in which particles of alloys with an amorphous structure play the role of reinforcement. During the fabrication of these composites, a crystalline metal is in contact with a multicomponent alloy of an amorphous structure. In the present work, the morphological features of the reaction products formed upon the interaction of Fe$_{66}$Cr$_{10}$Nb$_5$B$_{19}$ metallic glass particles with aluminum were studied. The composites were processed via spark plasma sintering (SPS), hot pressing or a combination of SPS and furnace annealing. The reaction products in composites with different concentrations of the metallic glass and different transformation degrees were examined. The products of the interaction of the Fe$_{66}$Cr$_{10}$Nb$_5$B$_{19}$ metallic glass with Al were observed as dense layers covering the residual alloy cores, needles of FeAl$_3$ protruding from the dense shells as well as needles and platelets of FeAl$_3$ distributed in the residual Al matrix. The possible role of the liquid phase in the structure formation of the reaction products is discussed. The formation of needle- and platelet-shaped particles presumably occurred via crystallization from the Al-Fe-based melt, which formed locally due to the occurrence of the exothermic reactions between aluminum and iron. At the same time, aluminum atoms diffused into the solid Fe-based alloy particles, forming an intermetallic layer, which could grow until the alloy was fully transformed. When aluminum melted throughout the volume of the composite during heating of the sample above 660 °C, a similar microstructure developed. In both Al–Fe$_{66}$Cr$_{10}$Nb$_5$B$_{19}$ and Al–Fe systems, upon the reactive transformation, pores persistently formed in locations occupied by aluminum owing to the occurrence of the Kirkendall effect.

Keywords: metallic glass; interface; aluminum; intermetallics; morphology; diffusion

1. Introduction

Traditional reinforcements in metal matrix composites (MMCs) are particles or fibers of crystalline nature. The promising alternative reinforcements are metallic glasses [1–3]. In metallic-glass-reinforced MMC, a crystalline metal is in contact with a metastable phase, a multicomponent alloy of an amorphous structure. Such systems are of fundamental interest as they present opportunities for studying the chemical interactions between

a crystalline metal and an amorphous alloy [4–8]. Metallic glasses can act as glues for materials of different nature [9]. The crystalline and amorphous alloys can be joined together at low temperatures (for example, using high-frequency vibrations [10,11]) and upon heat treatment, such as sintering [3].

Interfaces are key elements of composite structures, ensuring their integrity and enabling the load transfer from the matrix to the reinforcement. The interactions between the phases determine the crystallographic nature of the interface and the thickness and structure of the reaction product layers. The efficiency of the load transfer from the matrix to the reinforcement depends on the physical and chemical bonding at the interface. Furthermore, the layers of the reaction products become additional reinforcing elements of the composite [12]. The reactive transformations at the metallic glass/metal matrix interface can lead to the spatial redistribution of the alloy components owing to the formation of intermetallic phases. In ref. [4], the formation of a dual-layer structure (composed of two intermetallics) was observed when a Ni-Nb amorphous alloy reacted with aluminum.

Field-assisted sintering [13,14] is often the technology of choice for consolidating materials containing metastable phases. Spark plasma sintering (SPS) has been used for obtaining bulk materials from metallic glass–metal mixtures [15–19]. The inherent local phenomena related to the direct passage of an electric current through the system during SPS should be taken into account when the structure formation mechanisms are investigated [15]. As the glassy phase contains metals, the products of its interaction with the metal matrix are intermetallic phases or solid solutions. The newly formed layers should repeat the surface morphology of the glassy particles as the absence of the crystalline and grain structure eliminates the possibility of reaction advancement in preferable directions or channels. However, in some cases, the interface between the matrix and the reaction product layer is not very smooth, the layer demonstrating protrusions [15].

The $Fe_{66}Cr_{10}Nb_5B_{19}$ glassy alloy is an attractive composition for practical purposes, as it can be obtained from commercially available alloys and is lean in the alloying elements [20,21]. It features high hardness and high corrosion resistance [21]. In the past few years, we have conducted investigations of the structural characteristics and mechanical properties of composites obtained by SPS of Al–$Fe_{66}Cr_{10}Nb_5B_{19}$ power mixtures [17–19]. The mechanical properties of these composites were found to be very sensitive to their phase composition and microstructure.

The present work deals with the structural evolution of Al–$Fe_{66}Cr_{10}Nb_5B_{19}$ composites having different concentrations of the $Fe_{66}Cr_{10}Nb_5B_{19}$ metallic glass. The goal of the present work was to study the chemical interaction of the $Fe_{66}Cr_{10}Nb_5B_{19}$ metallic glass with aluminum and the morphology of the resultant structures. In the Al-Fe system, the Kirkendall effect is well known [22–24]. At the Al/Fe interface, a reaction product of intermetallic nature forms. Al diffuses through an intermetallic reaction product layer, leaving vacancies in the aluminum particles. The vacancies further coalesce, forming pores. The Kirkendall porosity was observed in the annealed aluminum–steel joints; the pores were interconnected, forming a seam at the Al/θ phase ($FeAl_3$) interface [25]. To the best of our knowledge, the Kirkendall effect in the Al–$Fe_{66}Cr_{10}Nb_5B_{19}$ system has not been previously reported. In this work, experiments were designed in such a way that the powder mixtures of the Al and $Fe_{66}Cr_{10}Nb_5B_{19}$ metallic glass reactants experienced high transformation degrees. This approach can help shed light on the mechanisms of the structural changes occurring during the fabrication of the composites by sintering and upon unexpected overheating during the performance.

2. Materials and Methods

Experiments were conducted with Al–$Fe_{66}Cr_{10}Nb_5B_{19}$ and Al-Fe powder mixtures. In order to prepare the mixtures, gas-atomized powders of $Fe_{66}Cr_{10}Nb_5B_{19}$ [20] (<45 μm and 20–40 μm fractions), an iron powder (carbonyl iron, particle size range 2.5–5 μm) and three aluminum powders (PAD-6, particle size range 3–10 μm; PAD-0, particle size range 3–30 μm; PA-4 grade, particle size range 10–45 μm) were used. All powders used in the

present work had a spherical shape. The Al–$Fe_{66}Cr_{10}Nb_5B_{19}$ and Al-Fe mixtures were prepared by treatment in a custom-made horizontal low-energy mixing device. The glass transition temperature of the glassy $Fe_{66}Cr_{10}Nb_5B_{19}$ alloy is 521 °C and its crystallization temperature is 573 °C (determined at a heating rate of 10 °C min^{-1}) [20]. The minor phase in the $Fe_{66}Cr_{10}Nb_5B_{19}$ powder is α-(Fe,Cr), which is present at a concentration of about 5 wt.% [26]. Sintering and annealing experiments described in the present work were conducted at temperatures above the crystallization temperature of the metallic glass.

Sintering of the powders was carried out using a SPS Labox 1575 apparatus (SINTER LAND Inc., Nagaoka, Japan) in vacuum at a uniaxial pressure of 40 MPa. Graphite tooling was used. The powder mixtures were placed in the dies 10 mm or 20 mm in diameter. The temperature during SPS was measured by a thermocouple inserted into a near-through hole in the die wall. The real temperature of the sintered sample is about 30 °C higher than the measured temperature for dies 10–20 mm in diameter in the temperature range of 500–600 °C, as determined experimentally by the onset of the rapid shrinkage of the $Fe_{66}Cr_{10}Nb_5B_{19}$ samples upon reaching the glass transition temperature. In the present work, the Al–$Fe_{66}Cr_{10}Nb_5B_{19}$ and Al-Fe mixtures were subjected to SPS at 570 °C, as measured by the thermocouple. The heating rate was 50 °C min^{-1}. The holding time at the maximum temperature was 3 min or 20 min. Due to the high heating rates and short sintering times during SPS, the alloy $Fe_{66}Cr_{10}Nb_5B_{19}$ remained mainly amorphous, and only the very beginning of its crystallization could be expected. Selected sintered samples were further annealed in a vacuum furnace for 2 h at a temperature of 620 °C.

The powders were also consolidated by hot pressing (HP) using a facility developed at the Institute of Automation and Electrometry SB RAS, Novosibirsk, Russia. HP was conducted in an atmosphere of argon. The heating rate was the same as in the SPS experiments. A Fe–Al (3:2, mol.) mixture was consolidated at 650 °C and 3 MPa. The Al–20 vol.% $Fe_{66}Cr_{10}Nb_5B_{19}$ mixture was heated up to 660 °C under a pressure of 40 MPa. The heating was switched off once rapid displacement started upon melting of the aluminum contained in the mixture.

X-ray diffraction (XRD) patterns of the samples were recorded by a D8 ADVANCE diffractometer (Bruker AXS, Karlsruhe, Germany) with Cu Kα radiation.
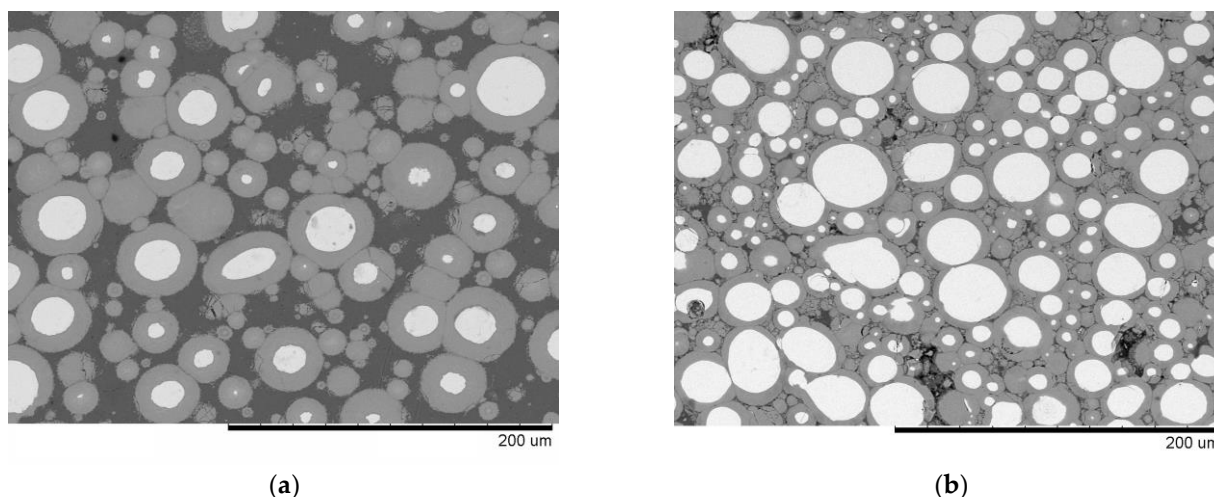
The microstructure of the sintered and annealed samples was studied using scanning electron microscopy (SEM) using a TM-1000 Tabletop microscope (Hitachi, Tokyo, Japan) and a S-3400N microscope (Hitachi, Tokyo, Japan). Both fracture and polished surfaces of the samples were observed. Energy-dispersive spectroscopy (EDS) was conducted using a NORAN Spectral System 7 (Thermo Fisher Scientific Inc., Waltham, MA, USA) attached to the S-3400N microscope. The EDS point and line analyses were conducted on the polished surfaces.

3. Results

3.1. Phase Composition and Microstructural Features of Materials Obtained by Spark Plasma Sintering of Al-$Fe_{66}Cr_{10}Nb_5B_{19}$ Powder Mixtures

Figure 1a shows the microstructure of materials obtained by SPS of the Al–20 vol.% $Fe_{66}Cr_{10}Nb_5B_{19}$ mixture at 570 °C. The composite consists of the core–shell particles distributed in the residual Al matrix. The shells are the reaction products between the aluminum and the Fe-based alloy. In the XRD pattern of this material (Figure 2a), reflections of Al, $FeAl_3$ and Fe_2Al_5 can be distinguished. It should be noted that the exact formula of the Al-rich phase in the Fe-Al system is Fe_4Al_{13} [27,28]. However, in many publications related to the thermodynamic aspects, the synthesis of composites and the interfacial interaction between Al and Fe, the $FeAl_3$ formula is still used.

related to the thermodynamic aspects, the synthesis of composites and the interfacial interaction between Al and Fe, the FeAl₃ formula is still used.
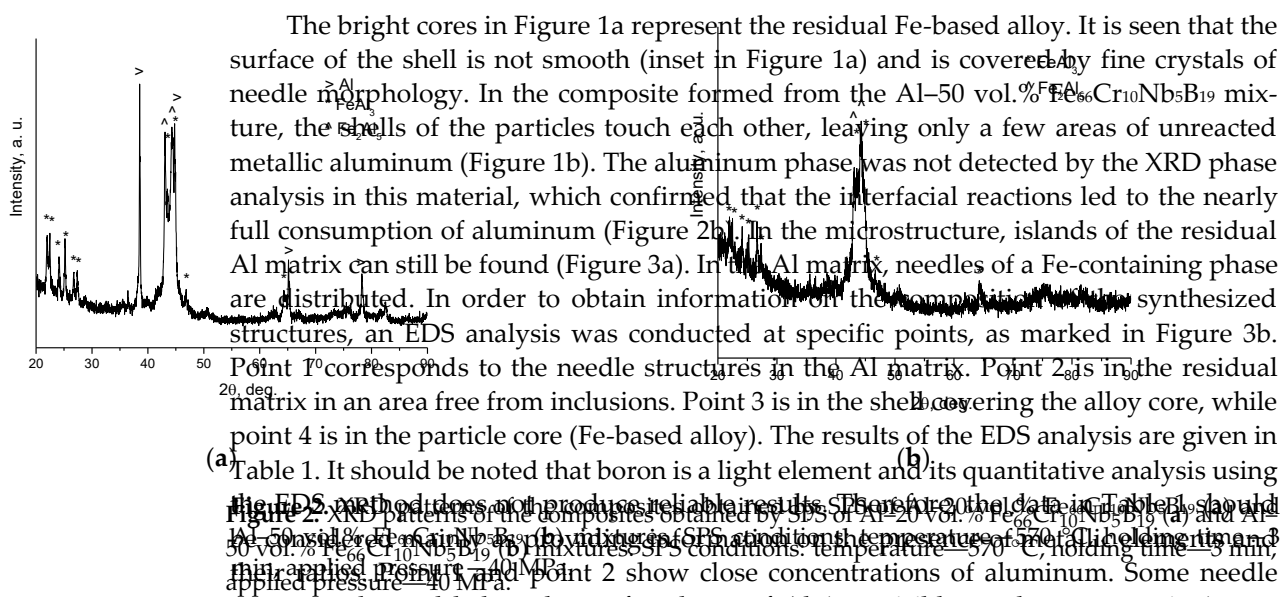
Figure 1. Microstructure of the composites obtained by spark plasma sintering (SPS) of Al–20 vol.% Fe₆₆Cr₁₀Nb₅B₁₉ (**a**) and Al–50 vol.% Fe₆₆Cr₁₀Nb₅B₁₉ (**b**) mixtures. The shell of a particle at a higher magnification (**c**). Al powder 3–10 µm. SPS conditions: temperature—570 °C, holding time—3 min, applied pressure—40 MPa. Back-scattered electron (BSE) images.
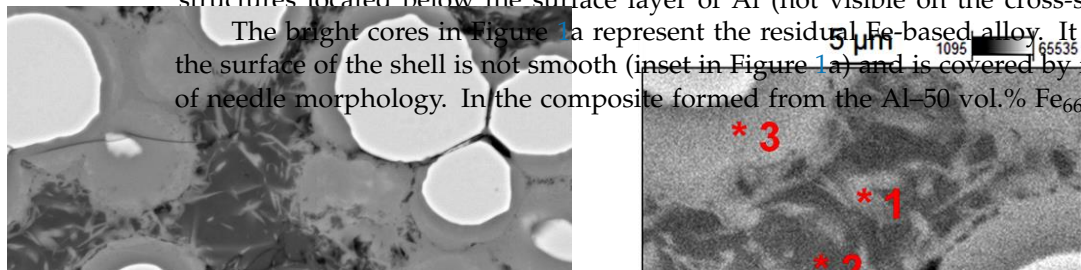
have contributed to the results of the analysis. The material in point 3 contained aluminum at a concentration that was slightly higher than that required to form the FeAl₃ (Fe₄Al₁₃) phase. Here, aluminum can participate in the formation of other intermetallics (of the Nb-Al and Cr-Al systems). However, they were present at concentrations that were too low to be detected by the XRD phase analysis.

The bright cores in Figure 1a represent the residual Fe-based alloy. It is seen that the surface of the shell is not smooth (inset in Figure 1a) and is covered by fine crystals of needle morphology. In the composite formed from the Al–50 vol.% Fe₆₆Cr₁₀Nb₅B₁₉ mixture, the shells of the particles touch each other, leaving only a few areas of unreacted metallic aluminum (Figure 1b). The aluminum phase was not detected by the XRD phase analysis in this material, which confirmed that the interfacial reactions led to the nearly full consumption of aluminum (Figure 2b). In the microstructure, islands of the residual Al matrix can still be found (Figure 3a). In the Al matrix, needles of a Fe-containing phase are distributed. In order to obtain information on the composition of the synthesized structures, an EDS analysis was conducted at specific points, as marked in Figure 3b. Point 1 corresponds to the needle structures in the Al matrix. Point 2 is in the residual matrix in an area free from inclusions. Point 3 is in the shell covering the alloy core, while point 4 is in the particle core (Fe-based alloy). The results of the EDS analysis are given in Table 1. It should be noted that boron is a light element and its quantitative analysis using the EDS method does not produce reliable results. Therefore, the data in Table 1 should be considered mainly qualitatively.

Figure 2. XRD patterns of the composites obtained by SPS of Al–20 vol.% Fe₆₆Cr₁₀Nb₅B₁₉ (**a**) and Al–50 vol.% Fe₆₆Cr₁₀Nb₅B₁₉ (**b**) mixtures. SPS conditions: temperature—570 °C, holding time—3 min, applied pressure—40 MPa.

Point 1 and point 2 show close concentrations of aluminum. Some needle structures located below the surface layer of Al (not visible on the cross-section) may

The bright cores in Figure 1a represent the residual Fe-based alloy. It is seen that the surface of the shell is not smooth (inset in Figure 1a) and is covered by fine crystals of needle morphology. In the composite formed from the Al–50 vol.% Fe₆₆Cr₁₀Nb₅B₁₉

mixture, the shells of the particles touch each other, leaving only a few areas of unreacted metallic aluminum (Figure 1b). The aluminum phase was not detected by the XRD phase analysis in this material, which confirmed that the interfacial reactions led to the nearly full consumption of aluminum (Figure 2b). In the microstructure, islands of the residual Al matrix can still be found (Figure 3a). In the Al matrix, needles of a Fe-containing phase are distributed. In order to obtain information on the composition of the synthesized structures, an EDS analysis was conducted at specific points, as marked in Figure 3b. Point 1 corresponds to the needle structures in the Al matrix. Point 2 is in the residual matrix in an area free from inclusions. Point 3 is in the shell covering the alloy core, while point 4 is in the particle core (Fe-based alloy). The results of the EDS analysis are given in Table 1. It should be noted that boron is a light element and its quantitative analysis using the EDS method does not produce reliable results. Therefore, the data in Table 1 should be considered mainly as providing information on the presence of metallic elements and their ratios. Point 1 and point 2 show close concentrations of aluminum. Some needle structures located below the surface layer of Al (not visible on the cross-section) may have contributed to the results of the analysis. The material in point 3 contained aluminum at a concentration that was slightly higher than that required to form the $FeAl_3$ (Fe-Al) phase. Here, aluminum can participate in the formation of other intermetallics (Nb-Al and Cr-Al systems). However, they were present at concentrations that were too low to be detected by the XRD phase analysis. In point 4, Al was not found, and the Fe/Cr atomic ratio was 6.2, which is close to that in the starting alloy.
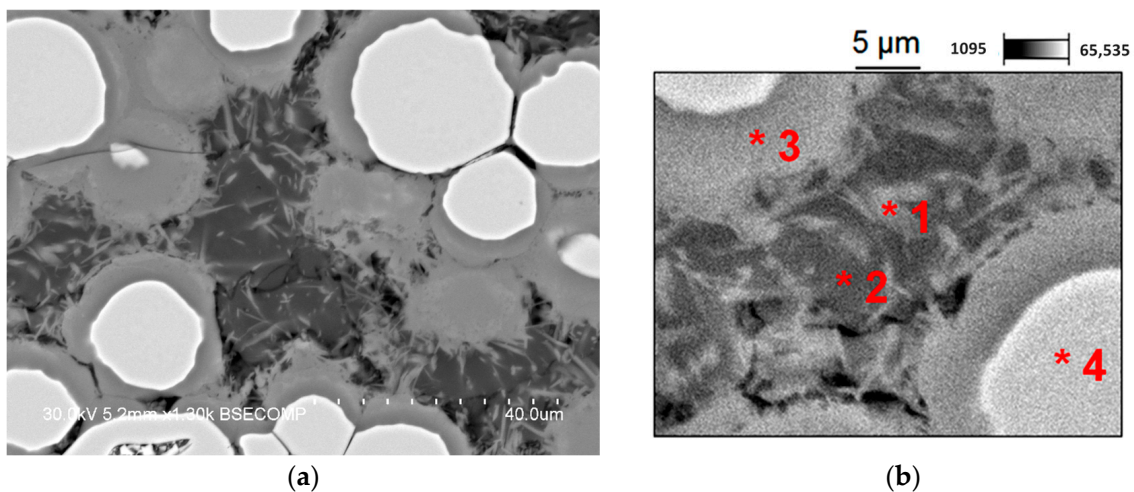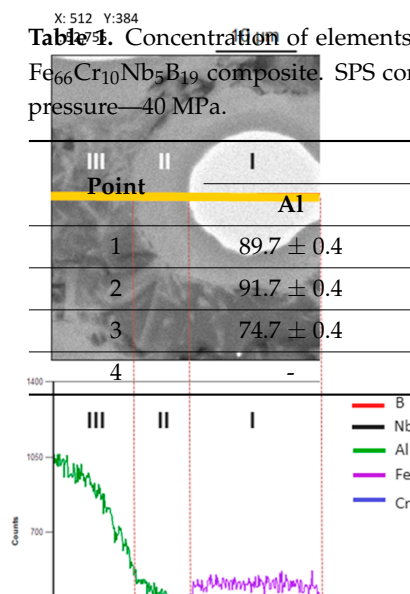

(a)   (b)

Figure 3. An area of the cross-section of the composite obtained by SPS of Al-50 vol.% $Fe_{66}Cr_{10}Nb_5B_{19}$ (**a**). SPS conditions: temperature—570 °C, holding time—3 min, applied pressure—40 MPa. The points (1, 2, 3 and 4) in which the energy dispersive spectroscopy (EDS) analysis was conducted are marked in (**b**). BSE images.

Table 1. Concentration of elements in points 1–4 marked in Figure 3b. Data for the Al–50 vol.% $Fe_{66}Cr_{10}Nb_5B_{19}$ composite. SPS conditions: temperature—570 °C, holding time—3 min, applied pressure—40 MPa.

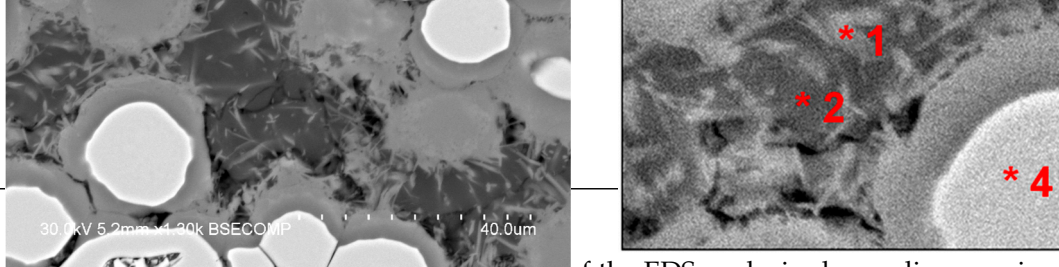| Point	Concentration, at.%				
	Al	**Fe**	**Cr**	**Nb**	**B**
1	89.7 ± 0.4	9.4 ± 0.1	0.9 ± 0.1	-	-
2	91.7 ± 0.4	7.1 ± 0.1	1.2 ± 0.1	-	-
3	74.7 ± 0.4	20.3 ± 0.2	4.4 ± 0.1	0.6 ± 0.4	-
4	-	80.2 ± 0.5	12.9 ± 0.2	2.2 ± 0.7	4.7 ± 1.9

Figure 4 shows the results of the EDS analysis along a line crossing a particle core (region I), a shell of the reaction products (region II) and a residual matrix region (III). This analysis helps to visualize the concentration changes along a line crossing two interfaces. The material in region I did not contain Al. In region II, Al, Fe and Cr were present. The presence of iron was also detected beyond the particle shell (region III). Signals coming from boron and niobium were very weak and were at the background level.
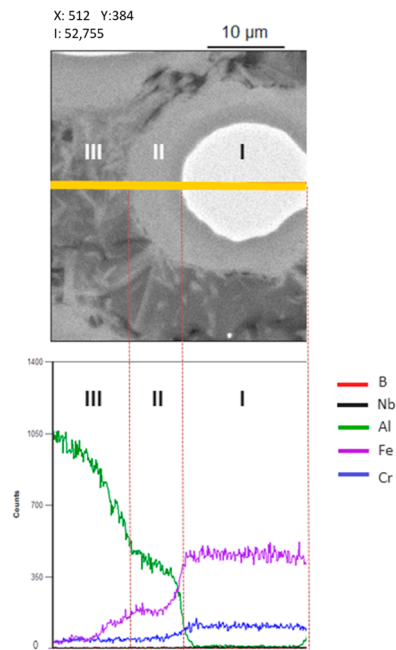

Figure 4. Line EDS of a partially reacted alloy particle in the residual Al matrix in the composite obtained by SPS of Al–50 vol.% Fe$_{66}$Cr$_{10}$Nb$_5$B$_{19}$. SPS conditions: temperature—570 °C, holding time—3 min, applied pressure—40 MPa.

For the purpose of a comparative analysis, an experiment in the hot press was conducted, during which aluminum melted throughout the volume of the composite, partially squeezing out of the die. As seen in Figure 5, the microstructural features of the obtained material were very similar to those formed during SPS at a measured temperature of 570 °C (Figures 1 and 3a): the products of interaction were visible in the form of a layer (the particle shell) and crystals of a needle shape.

In Figure 1b, pores can be seen between the particles of the core–shell structure, which implies that the diffusion of the aluminum into the alloy occurred faster than the diffusion of the alloy components into the aluminum. In order to obtain further confirmation of the preferential diffusion of the aluminum into the alloy particles, sintering of an Al–70 vol.% Fe$_{66}$Cr$_{10}$Nb$_5$B$_{19}$ mixture was carried out. A low concentration of aluminum in this mixture allowed us to obtain a structure in which the Al particles were surrounded by the metallic glass matrix. An Al powder with particles larger than those of the metallic glass was used for the preparation of the mixture. This allowed us to distinguish pores formed due to the Kirkendall effect and those formed because of the incomplete sintering of the glass particles by their size. Figure 6 demonstrates the fracture surface of the sintered material fabricated from the Al–70 vol.% Fe$_{66}$Cr$_{10}$Nb$_5$B$_{19}$ mixture. In this material, Al fully transformed into the intermetallic phases, as confirmed by the XRD analysis (Figure 7). The pores formed in locations of the Al particles throughout the compact (Figure 6a). It is seen that the walls of the pores were covered with needles (Figure 6b).
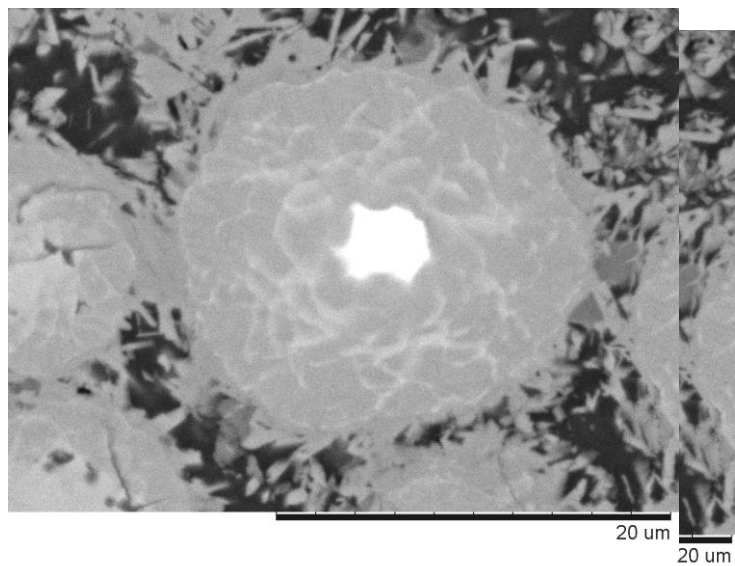
Figure 5. A core–shell particle in the microstructure of the composite formed during heating of the Al–20 vol.% Fe66Cr10Nb5B19 mixture in the hot press. HP conditions: temperature—above 660 °C, applied pressure—40 MPa. BSE image.
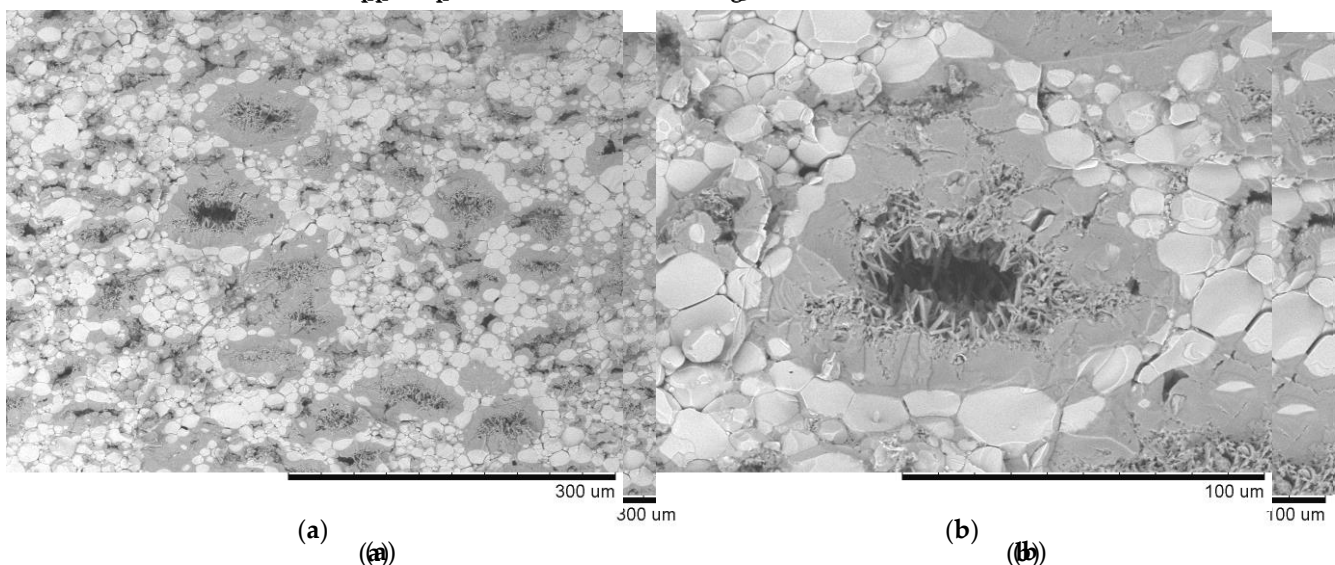
(**a**) (**b**)

Figure 6. Fracture surface of the material obtained by SPS of Al–70 vol.% Fe66Cr10Nb5B19, (**a**,**b**) different magnifications. All powder 10–45 um. SPS conditions: temperature—570 °C, holding time—20 min, applied pressure—40 MPa. BSE images.
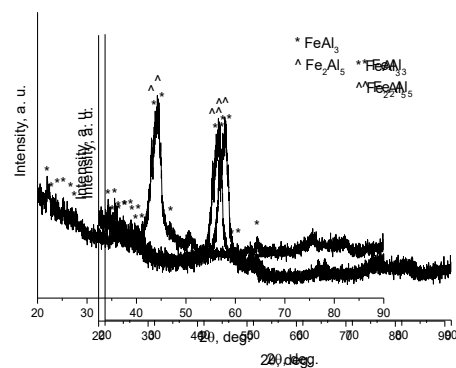
Figure 7. XRD pattern of the material obtained by SPS of Al–70 vol.% Fe66Cr10Nb5B19. SPS conditions: temperature—570 °C, holding time—20 min, applied pressure—40 MPa.

3.2. Structural Changes during Annealing of Preconsolidated Al-Fe$_{66}$Cr$_{10}$Nb$_5$B$_{19}$ Compacts

The formation of pores can be better traced if the compacts are heated without the application of pressure. The composite spark plasma sintered from the Al-20 vol.% Fe$_{66}$Cr$_{10}$Nb$_5$B$_{19}$ mixture (Figure 8a) was annealed in a furnace at 620 °C for 2 h. After SPS, no reaction product was present in the material, as confirmed by the XRD (Figure 9a). The fracture surface of the material formed after annealing is shown in Figure 8b. It is seen that the material was porous and was composed of nearly spherical particles surrounded by platelets and needle-shape crystals. In some cases, the roughly parthole was partially prestled (Figure 8c). The morphology of the needle-shape crystals present in the present is shown in Figure 8d. As seen in the XRD pattern in Figure 9b, during annealing the alloy reacted with the Al to form Fe$_2$Al$_3$, FeAl$_3$ and Fe$_2$Al$_5$ phases.

(**a**)

(**b**)

(**c**)

(**d**)
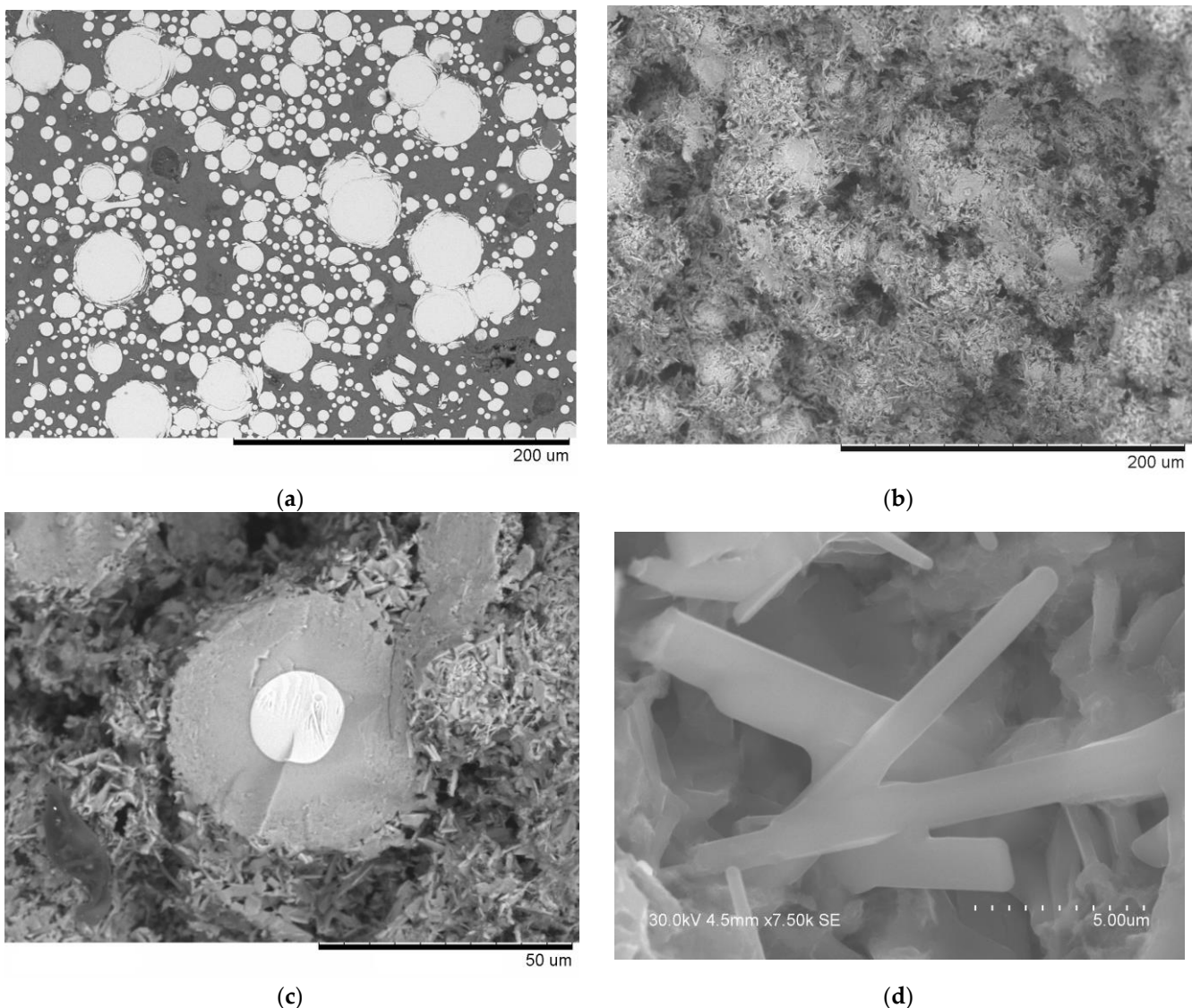
Figure 8. (**a**) Microstructure of the composite obtained by SPS of Al-20 vol.% Fe$_{66}$Cr$_{10}$Nb$_5$B$_{19}$. Al powder 3–10 μm. SPS conditions: temperature—500 °C, holding time—3 min, applied pressure—40 MPa. (**b**) Fracture surface of the composite obtained by SPS and further annealed at 620 °C for 2 h. (**c**) An area of the fracture surface showing an unreacted Fe-based alloy core surrounded by platelets and needles of the intermetallic products. (**d**) The product of interaction with needle morphology. (**a–c**) BSE images. (**d**) Secondary electron (SE) image.
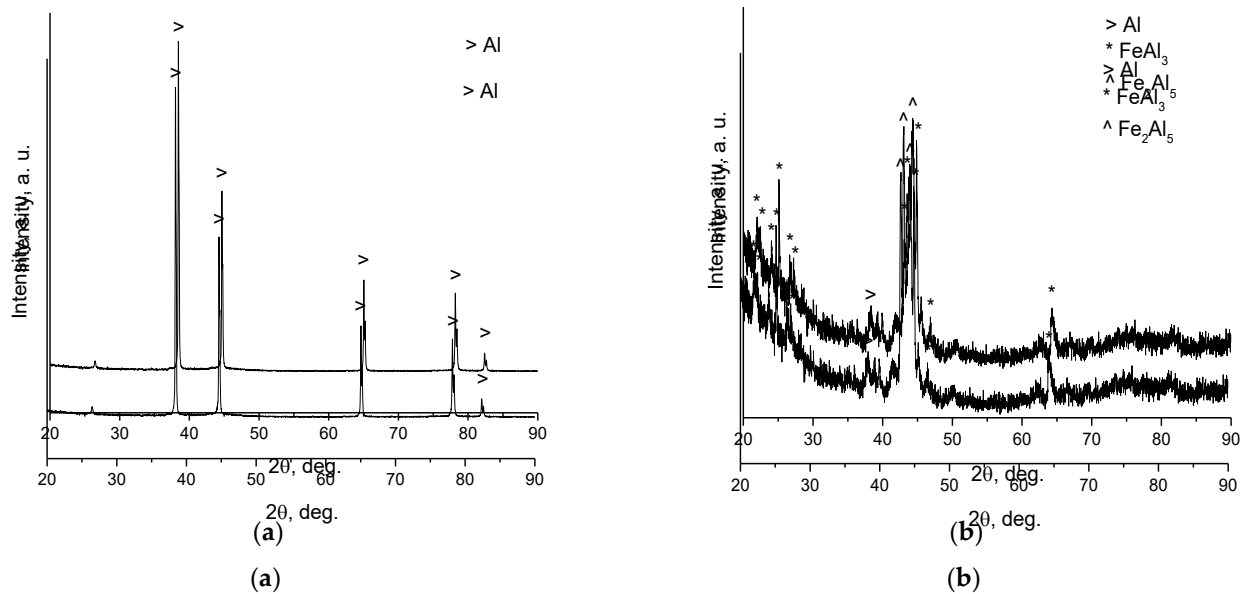
(a)

(b)

Figure 9. (**a**) XRD pattern of the composite obtained by SPS of Al–50 vol.% Fe$_{66}$Cr$_{10}$Nb$_5$B$_{19}$. SPS conditions: temperature—500 °C, holding time—3 min, applied pressure—40 MPa. (**b**) XRD pattern of the composite obtained by SPS and further annealed in vacuum at 620 °C for 2 h.

3.3. Microstructure of Materials Consolidated from Al-Fe Mixtures

In order to confirm the leading role of the interaction between aluminum and iron of the alloy in the structural changes in the composites upon sintering and annealing, experiments were conducted with Al-Fe mixtures. Figure 10a shows the microstructure of the materials sintered from an Al-Fe mixture having the same atomic ratio (4:1) as the Al–20 vol.% Fe$_{66}$Cr$_{10}$Nb$_5$B$_{19}$ composite. In this material, the FeAl$_3$ and Fe$_2$Al$_5$ phases formed (Figure 11a). Along with equiaxed grains, platelet-shape (needle) particles were seen in the microstructure.

(a)
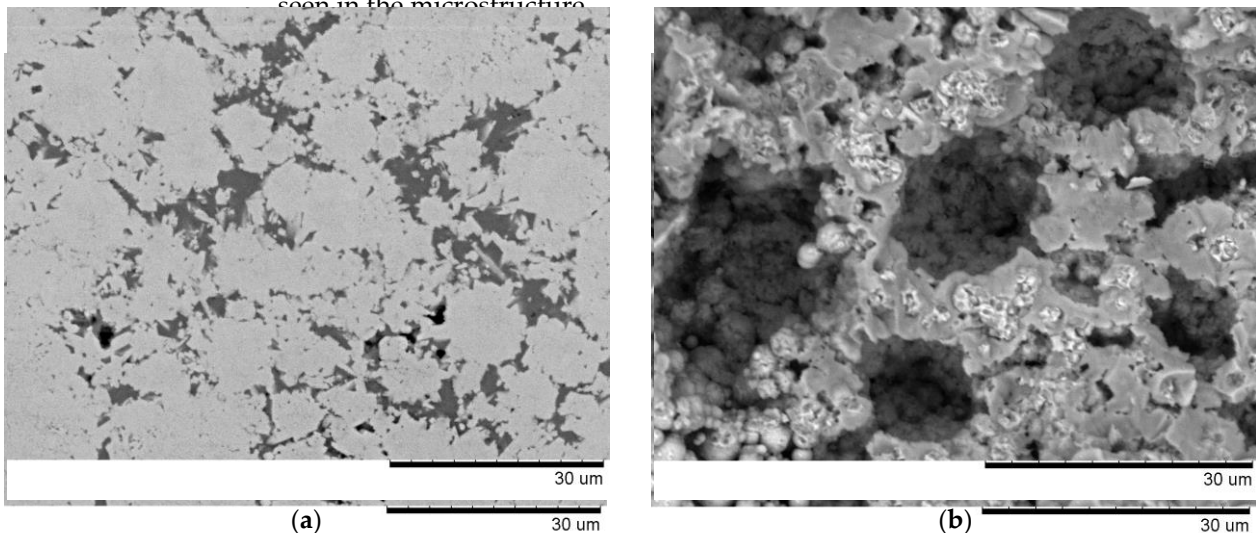
(b)

Figure 10. (**a**) Microstructure of the material obtained by SPS of Al-Fe (4:1 mol.) mixture. Al powder 3–10 µm. SPS conditions: temperature—570 °C, holding time—3 min, applied pressure—40 MPa. (**b**) Fracture surface of the material obtained by HP of the Al-Fe (3:2 mol.). Al powder 3–30 µm. HP conditions: temperature—650 °C, holding time—5 min, applied pressure—3 MPa. BSE images.

(**a**)   (**b**)

Figure 11. (**a**) XRD pattern of the material obtained by SPS of Al-Fe (4:1 mol.) mixture. SPS conditions: temperature—570 °C, holding time—3 min, applied pressure—40 MPa. (**b**) XRD pattern of the material obtained by HP of the Al-Fe mixture (3:2 mol.). HP conditions: temperature—650 °C, holding time—5 min, applied pressure—3 MPa.

The formation of pores during sintering of the Al-Fe mixture under a low applied pressure was also confirmed (Figure 10b). At the selected processing temperature (650 °C), particles of iron and those of the synthesized Fe-Al intermetallics could not be sintered well. Therefore, a low applied pressure was used (3 MPa) to prevent damaging the skeleton and making it easier to observe the pores formed due to the Kirkendall effect. Pores 15–20 μm in diameter formed in locations of the Al particles. The walls of the porous skeleton were composed of iron and the intermetallic phases, and metallic aluminum was no longer present in the material (Figure 11b).

4. Discussion

The morphologies of the reaction products in the samples obtained by SPS and annealing accompanied by the reactive transformation demonstrated similarities (Figures 1, 3a, 5, 6b, 8c,d). It can be inferred that the needle and platelet morphologies were not characteristic of the certain sintering method. Rather, they were a feature of the reaction system, in which the ratio of Al/Fe was 3:1 or greater, at least locally and for a certain period of time (time of the experiment). Zhang et al. [29] discussed the possible morphology of the FeAl₃ crystals, pointing to the fact that the needle and platelet morphology was typical for this intermetallic compound because of its low symmetry. The morphology of the proeutectic FeAl₃ was found to depend on the cooling rate.

In the discussion of the influence of the processing parameters on the morphological features of the reaction products, the possibility of the formation of a liquid phase during the processing of the composites needs to be addressed. For composites obtained by SPS, the possibility of local overheating at the interparticle contacts exists and has been demonstrated for a number of systems [30,31]. So, the temperature uncertainty and the possibility of the local solid/liquid interaction at the interparticle contacts exist and have been demonstrated for the interaction of the Fe₆₆Cr₁₀Nb₅B₁₉ metallic glass with aluminum and should be possible for dealing solid/liquid interaction in the formation of the Fe-Al intermetallics promoted by SPS. But the temperature in the reaction zone can be higher than the set temperature. The standard heat of formation of the FeAl₃ and Fe₂Al₅ compounds is 112 kJ/mol and 188 kJ/mol (values are exothermic compound), respectively [30]. The adiabatic combustion temperature of the reaction system transforming into FeAl₃ is 1127 K and the case of Fe₂Al₅ it is 1284 K. Therefore, under conditions realized in the present work, the following mechanisms of the formation of the FeAl₃ intermetallic can be suggested. The initiation of

the reaction between the alloy and aluminum resulting in the formation of $FeAl_3$ leads to a release of heat, which causes a local rise in temperature and melting of aluminum in the vicinity of the reaction site. Iron atoms from the glass can diffuse into liquid aluminum. The formation of faceted $FeAl_3$ crystals and needle-like structures occurs via crystallization from the Al-Fe-based melt upon cooling. At the same time, the aluminum atoms diffuse into the alloy and a $FeAl_3$-based layer grows until the alloy is fully transformed. When cast iron corrodes in molten aluminum, a similar situation develops [33]. An Al-containing layer forms at the interface between the cast iron and the melt, while some iron dissolves into aluminum, which leads to the formation of $FeAl_3$ needles in the aluminum matrix at a distance from the interface. The needles can also peel off the surface [30]. The formation of $FeAl_3$ needles emanating directly from the shell of the particles in this work is consistent with results of Guan et al. [15], who reported the formation of protrusions (prominences) composed of $FeAl_3$ at the interface between Fe-based metallic glass particles and aluminum in composites processed by SPS and hot rolling. It is possible to assume that such structures grow by means of the mechanism operating during the growth of whiskers from a layer experiencing compressive stresses upon the inward diffusion of species and the formation of an intermetallic compound [34].

The kinetics of the reaction of a solid spherical particle with smaller particles of another reactant can be described by a model developed by Carter [35]. In that model, the difference between the volume of the product and volume of the reactant consumed in the process is taken into account. The conversion degree is a key parameter in that model. In the present work, it was not possible to determine the exact conversion degree of the alloy by the XRD. If an Al-Fe alloy contains $FeAl_3$ and Fe_2Al_5 phases, its analysis by the XRD becomes difficult, as reflections of these phases partially overlap [36]. Furthermore, the presence of four elements in the alloy complicates the kinetic analysis. In practice, it is rather difficult to obtain monosized spheres of the glassy alloy. The above considerations show that morphological studies and the experimental determination of the phase composition of the composites are of utmost importance for assessing their thermal stability and understanding their structural evolution upon heat treatment.

5. Conclusions

The morphological features of the products of the reaction between the $Fe_{66}Cr_{10}Nb_5B_{19}$ metallic glass and aluminum were examined. A series of composite samples were fabricated/annealed at measured (bulk) temperatures below the aluminum melting point.

The structural investigations allowed us to assume that the growth of the $FeAl_3$ particles of needle and platelet morphologies occurred via crystallization from the Al-Fe-based melt, which formed locally due to the exothermic reactions between aluminum and iron. During SPS, the material can melt at the interparticle contacts, which is a feature of the electric-current-assisted sintering.

Aluminum atoms also diffused into the solid Fe-based alloy particles, enabling the growth of an intermetallic layer until the alloy particle was fully transformed. A similar microstructure developed when the composite was heated above 660 °C and the alloy particles reacted with molten aluminum.

In both Al–$Fe_{66}Cr_{10}Nb_5B_{19}$ and Al–Fe systems, upon the reactive transformation, pores persistently formed in locations occupied by the aluminum particles owing to the occurrence of the Kirkendall effect.

References

1. Dudina, D.V.; Georgarakis, K.; Yavari, A.R. Metal matrix composites reinforced with metallic glass particles: State of the art. In *Metal Matrix Composites*; Davim, J.P., Ed.; Nova Science Publishers, Inc.: New York, NY, USA, 2012; pp. 1–30.
2. Jayalakshmi, S.; Arvind Singh, R.; Gupta, M. Metallic glasses as potential reinforcements in Al and Mg matrices: A review. *Technologies* **2018**, *6*, 40. [CrossRef]
3. Georgarakis, K.; Dudina, D.V.; Kvashnin, V.I. Metallic glass-reinforced metal matrix composites: Design, interfaces and properties. *Materials* **2022**, *15*, 8278. [CrossRef] [PubMed]
4. Yu, P.; Zhang, L.C.; Zhang, W.Y.; Das, J.; Kim, K.B.; Eckert, J. Interfacial reaction during the fabrication of $Ni_{60}Nb_{40}$ metallic glass particles-reinforced Al based MMCs. *Mater. Sci. Eng. A* **2007**, *444*, 206–213. [CrossRef]
5. Yu, P.; Venkataraman, S.; Das, J.; Zhang, L.C.; Zhang, W.; Eckert, J. Effect of high pressure during the fabrication on the thermal and mechanical properties of amorphous $Ni_{60}Nb_{40}$ particle-reinforced Al-based metal matrix composites. *J. Mater. Res.* **2007**, *22*, 1168–1173. [CrossRef]
6. Wang, Z.; Georgarakis, K.; Nakayama, K.S.; Li, Y.; Tsarkov, A.A.; Xie, G.; Dudina, D.; Louzguine-Luzgin, D.V.; Yavari, A.R. Microstructure and mechanical behavior of metallic glass fiber-reinforced Al alloy matrix composites. *Sci. Rep.* **2016**, *6*, 24384. [CrossRef]
7. Avettand-Fènoël, M.N.; Netto, N.; Simar, A.; Marinova, M.; Taillard, R. Design of a metallic glass dispersion in pure copper by friction stir processing. *J. Alloys Compd.* **2022**, *907*, 164522. [CrossRef]
8. Wu, G.; Liu, C.; Brognara, A.; Ghidelli, M.; Bao, Y.; Liu, S.; Wu, X.; Xia, W.; Zhao, H.; Rao, J.; et al. Symbiotic crystal-glass alloys via dynamic chemical partitioning. *Mater. Today* **2021**, *51*, 6–14. [CrossRef]
9. Fu, J.; Yang, J.; Wu, K.; Lin, H.; Wen, W.; Ruan, W.; Ren, S.; Zhang, Z.; Liang, X.; Ma, J. Metallic glue for designing composite materials with tailorable properties. *Mater. Horiz.* **2021**, *8*, 1690–1699. [CrossRef]
10. Zhang, J.Y.; Zhou, Z.Q.; Zhang, Z.B.; Park, M.H.; Yu, Q.; Li, Z.; Ma, J.; Wang, A.D.; Huang, H.G.; Song, M.; et al. Recent development of chemically complex metallic glasses: From accelerated compositional design, additive manufacturing to novel applications. *Mater. Futur.* **2022**, *1*, 012001. [CrossRef]
11. Liang, X.; Zhu, X.; Li, X.; Mo, R.; Liu, Y.; Wu, K.; Ma, J. High-entropy alloy and amorphous alloy composites fabricated by ultrasonic vibrations. *Sci. China Phys. Mech. Astron.* **2020**, *63*, 116111. [CrossRef]
12. Dudina, D.V.; Georgarakis, K. Core–shell particle reinforcements—A new trend in the design and development of metal matrix composites. *Materials* **2022**, *15*, 2629. [CrossRef]
13. Olevsky, E.A.; Dudina, D.V. *Field-Assisted Sintering: Science and Applications*; Springer International Publishing: Cham, Switzerland, 2018; 425p.
14. Dudina, D.V.; Georgarakis, K.; Olevsky, E.A. Progress in aluminium and magnesium matrix composites obtained by spark plasma, microwave and induction sintering. *Int. Mater. Rev.* **2022**, *in press*. [CrossRef]
15. Guan, H.D.; Li, C.J.; Gao, P.; Prashanth, K.G.; Tan, J.; Eckert, J.; Tao, J.M.; Yi, J.H. Aluminum matrix composites reinforced with metallic glass particles with core-shell structure. *Mater. Sci. Eng. A* **2020**, *771*, 138630. [CrossRef]
16. Wang, Z.; Xie, M.S.; Zhang, W.W.; Yang, C.; Xie, G.Q.; Louzguine-Luzgin, D.V. Achieving super-high strength in an aluminum based composite by reinforcing metallic glassy flakes. *Mater. Lett.* **2020**, *262*, 127059. [CrossRef]
17. Dudina, D.V.; Bokhonov, B.B.; Batraev, I.S.; Amirastanov, Y.N.; Ukhina, A.V.; Kuchumova, I.D.; Legan, M.A.; Novoselov, A.N.; Gerasimov, K.B.; Bataev, I.A.; et al. Interaction between $Fe_{66}Cr_{10}Nb_5B_{19}$ metallic glass and aluminum during spark plasma sintering. *Mater. Sci. Eng. A* **2021**, *799*, 140165. [CrossRef]
18. Dudina, D.V.; Bokhonov, B.B.; Batraev, I.S.; Kvashnin, V.I.; Legan, M.A.; Novoselov, A.N.; Anisimov, A.G.; Esikov, M.A.; Ukhina, A.V.; Matvienko, A.A.; et al. Microstructure and mechanical properties of composites obtained by spark plasma sintering of Al–$Fe_{66}Cr_{10}Nb_5B_{19}$ metallic glass powder mixtures. *Metals* **2021**, *11*, 1457. [CrossRef]
19. Kvashnin, V.I.; Dudina, D.V.; Ukhina, A.V.; Koga, G.Y.; Georgarakis, K. The benefit of the glassy state of reinforcing particles for the densification of aluminum matrix composites. *J. Compos. Sci.* **2022**, *6*, 135. [CrossRef]
20. Kuchumova, I.D.; Batraev, I.S.; Ulianitsky, V.Y.; Shtertser, A.A.; Gerasimov, K.B.; Ukhina, A.V.; Bulina, N.V.; Bataev, I.A.; Koga, G.Y.; Guo, Y.; et al. Formation of metallic glass coatings by detonation spraying of a $Fe_{66}Cr_{10}Nb_5B_{19}$ powder. *Metals* **2019**, *9*, 846. [CrossRef]

21. Koga, G.Y.; Ferreira, T.; Guo, Y.; Coimbrão, D.D.; Jorge, A.M., Jr.; Kiminami, C.S.; Bolfarini, C.; Botta, W.J. Challenges in optimizing the resistance to corrosion and wear of amorphous Fe-Cr-Nb-B alloy containing crystalline phases. *J. Non-Cryst. Solids* **2021**, *555*, 120537. [CrossRef]

22. Salamon, M.; Mehrer, H. Interdiffusion, Kirkendall effect, and Al self-diffusion in iron–aluminium alloys. *Z. Für Met.* **2005**, *96*, 4–16. [CrossRef]

23. Gao, H.; He, Y.; Shen, P.; Zou, J.; Xu, N.; Jiang, Y.; Huang, B.; Liu, C.T. Porous FeAl intermetallics fabricated by elemental powder reactive synthesis. *Intermetallics* **2009**, *17*, 1041–1046. [CrossRef]

24. Gao, H.Y.; He, Y.H.; Shen, P.Z.; Jiang, Y.; Liu, C.T. Effect of pressure on pore structure of porous FeAl intermetallics. *Adv. Powder Technol.* **2015**, *26*, 882–886. [CrossRef]

25. Springer, H.; Kostka, A.; dos Santos, J.F.; Raabe, D. Influence of intermetallic phases and Kirkendall-porosity on the mechanical properties of joints between steel and aluminium alloys. *Mater. Sci. Eng. A* **2011**, *528*, 4630–4642. [CrossRef]

26. Kuchumova, I.D.; Batraev, I.S.; Ukhina, A.V.; Borisenko, T.A.; Bulanova, U.E.; Ulianitsky, V.Y.; Dudina, D.V.; Shikalov, V.S.; Kosarev, V.F.; Bataev, I.A.; et al. Processing of Fe-based alloys by detonation spraying and spark plasma sintering. *J. Therm. Spray Tech.* **2021**, *30*, 1692–1702. [CrossRef]

27. Li, X.; Scherf, A.; Heilmaier, M.; Stein, F. The Al-rich part of the Fe-Al phase diagram. *J. Phase Equil. Diff.* **2016**, *37*, 162–173. [CrossRef]

28. Van Alboom, A.; Lemmens, B.; Breitbach, B.; De Grave, E.; Cottenier, S.; Verbeken, K. Multi-method identification and characterization of the intermetallic surface layers of hot-dip Al-coated steel: FeAl$_3$ or Fe$_4$Al$_{13}$ and Fe$_2$Al$_5$ or Fe$_2$Al$_{5+x}$. *Surf. Coat. Technol.* **2017**, *324*, 419–428. [CrossRef]

29. Zhang, N.; Hu, Q.; Ding, Z.; Lu, W.; Yang, F.; Li, J. 3D morphological evolution and growth mechanism of proeutectic FeAl$_3$ phases formed at Al/Fe interface under different cooling rates. *J. Mater. Sci. Technol.* **2022**, *116*, 83–93. [CrossRef]

30. Dudina, D.V.; Vidyuk, T.M.; Gavrilov, A.I.; Ukhina, A.V.; Bokhonov, B.B.; Legan, M.A.; Matvienko, A.A.; Korchagin, M.A. Separating the reaction and spark plasma sintering effects during the formation of TiC–Cu composites from mechanically milled Ti–C–3Cu mixtures. *Ceram. Int.* **2021**, *47*, 12494–12504. [CrossRef]

31. Dudina, D.V.; Grigoreva, T.F.; Devyatkina, E.T.; Vosmerikov, S.V.; Ukhina, A.V.; Markushin, V.V.; Lyakhov, N.Z. Structural features of tantalum carbide-copper composites obtained by liquid phase-assisted spark plasma sintering. *Ceram. Int.* **2022**, *48*, 32556–32560. [CrossRef]

32. Itin, V.I.; Naiborodenko, Y.S. *High-Temperature Synthesis of Intermetallic Compounds*; Tomsk State University Publishing: Tomsk, Russia, 1989; 214p. (In Russian)

33. Wang, Q.; Yang, H.; Li, X.; Zhang, G. Study of corrosion mechanism of cast iron in molten aluminum. *Mater. Res. Express* **2020**, *7*, 016534. [CrossRef]

34. Chason, E.; Jadhav, N.; Pei, F. Effect of layer properties on stress evolution, intermetallic volume, and density during tin whisker formation. *JOM* **2011**, *63*, 62. [CrossRef]

35. Carter, R.E. Kinetic model for solid-state reactions. *J. Chem. Phys.* **1961**, *34*, 2010–2015. [CrossRef]

36. Matysik, P.; Jóźwiak, S.; Czujko, T. Characterization of low-symmetry structures from phase equilibrium of Fe-Al system —Microstructures and mechanical properties. *Materials* **2015**, *8*, 914–931. [CrossRef] [PubMed]